DOI: 10.1002/adom.201902056
Article type: Full Paper

Narrowband-Absorption-Type Organic Photodetectors for the Far-Red Range based on Fullerene-Free Bulk Heterojunctions

*Kai Xia, Yachen Li, Yan Wang, Luis Portilla, Vincenzo Pecunia**

Jiangsu Key Laboratory for Carbon-Based Functional Materials & Devices, Institute of Functional Nano & Soft Materials (FUNSOM), Soochow University, 199 Ren'ai Road, Suzhou, 215123 Jiangsu, PR China

E-mail: vp293@suda.edu.cn

Keywords: narrowband organic photodetectors, non-fullerene acceptors, far-red photodetectors, narrowband-absorption photodetectors.

Spectrally-selective photodetection via organic semiconductors manifesting narrowband absorption (NBA photodetection) is highly attractive for emerging applications that require ultrathin, lightweight, and low-cost solutions. While successful over mainstream color bands, NBA photodetectors have struggled so far to meet the functional and/or performance demands at longer wavelengths, importantly in the far-red (700 – 750 nm), a range relevant to diverse applications in analytical biology, medical diagnostics, remote sensing, etc. Recognizing the potential of a non-fullerene-acceptor route to addressing this challenge, we explore the narrowband photodetection capabilities of SBDTIC, a recently-developed benzodithiophene-based acceptor with narrowband absorption in the far-red. We consider two bulk-heterojunction NBA configurations, in which SBDTIC is combined with a donor either absorbing also in the far-red, or transparent through the visible. We find that the latter configuration provides superior narrowband functionality, with peak detectivity of $1.42 \cdot 10^{13}$ Jones and spectral width of 141 nm—the highest detectivity to date for NBA far-red-selective photodetectors, and the smallest spectral width of all solution-processed implementations. In self-powered operation, such photodetectors additionally present a quasi-linear response over a photocurrent range of least four orders of magnitude, and respond in the microsecond range, further evidencing the suitability of this approach to address the wealth of target applications.

1. Introduction

Recent years have witnessed extensive research effort in developing photodetector technologies based on solution-processible semiconductors, in view of their facile processing, tailorable properties and potential low cost.[1–8] In particular, organic photodetectors with narrowband (or spectrally-selective) functionality have attracted ever-growing attention due to their potential beyond the confines of conventional photodetector technologies.[9–11] On the basis of their spectral tunability via chemical tailoring,[12] their facile low-temperature processing[13] and their mechanical flexibility,[14] organic semiconductors bear the promise of delivering narrowband photodetection with high performance and in unconventional settings and form factors,[15] e.g., in low-cost, point-of-use devices for wearable optoelectronics,[16,17] the Internet of Things,[18] computer vision,[19] and biomedicine.[20]

Among the several organic narrowband photodetection strategies that have been investigated to date, the so-called narrowband absorption (NBA) strategy—relying on a photoactive layer predominantly absorbing in the target spectral range—has been prominent.[11,15] Alternative narrowband strategies relying on internal optoelectronic filtering effects (such as charge carrier narrowing [21] and charge-injection narrowing[5,22]) or on microcavity resonance[23] have also been explored, delivering particularly remarkable performance for applications requiring a particularly narrow spectral response. With respect to the NBA strategy, it builds on the inherent spectral tunability and narrowband absorption of many organic semiconductors.[24–28] In particular, NBA photodetectors are inherently non-filtered, i.e., they have little/negligible impact on the spectral content of the incident light outside the target spectral range. Consequently, NBA photodetectors can potentially deliver multicolor/multispectral detection in a stacked configuration,[29–31] a route that is particularly attractive for high-resolution imaging beyond the capabilities of benchmark technologies. In fact, NBA photodetectors have been particularly successful in delivering narrowband functionality in the blue, green, and red

spectral regions, attaining spectral responsivity passbands with typical spectral widths of ≈ 100 – 150 nm, and specific detectivity values up to the 10^{13} Jones range.[11]

Developing and emerging applications (e.g., requiring multispectral capability) motivate the effort to expand the scope of organic NBA narrowband photodetectors beyond the boundaries of conventional color detection. In particular, narrowband photodetection in the far-red range (i.e., photodetectors with peak response at 700 – 750 nm)—dimly visible to the human eye and at the same time distinct from the infrared region—is of considerable interest, in view of its role in many natural processes and technological applications. Narrowband photodetection in the far-red range is relevant to analytical biology (e.g., flow cytometry[32]), medical diagnostics (e.g., brain imaging,[33] in-vivo tumor detection[34]), remote sensing,[35] botany,[36] precision agriculture,[37] and food quality inspection.[38] It is important to note that a large number of such applications require spectral widths loosely around 100 nm, in principle within reach of the NBA approach—while ultranarrowband passbands (spectral with ≲ 50 nm) would lead to poor photon collection, hence would be unsuitable for the purpose. In passing, we also note that many such application areas would greatly benefit from off-the-grid deployment, thus making photodetector operation in self-powered mode (*i.e.*, with 0 V as applied bias) highly desirable.

As confirmed by the paucity of the far-red NBA literature[27,39–43] (see also **Table S1** and our recent surveys of the field[11,15]), it has been challenging so far to replicate in the far-red range the success that the NBA strategy has achieved in the mainstream color bands. Indeed, the spectral width of far-red NBA photodetectors to date is typically approaching 200 nm or larger,[39–43] and in one instance the spectral rejection ratio is lower than 2,[39] i.e., the full width at half maximum is ill-defined (the spectral rejection ratio is intended as the ratio between the peak responsivity in the target spectral range and the responsivity outside the target spectral range[15]). This directly relates to the synthetic challenge of developing organic semiconductors that can selectively absorb in this spectral region without presenting additional absorption bands at shorter wavelengths in the visible range (which would worsen/compromise spectral rejection

in the stopband).[27,39,44–46] Adding to this challenge, organic photoactive layers are typically composed of two compounds, a donor and an acceptor, which are thus to jointly meet the spectral requirement mentioned earlier. In this respect, the adoption of fullerenes as acceptors—mainstream in organic optoelectronics—has been generally recognized as problematic for NBA photodetection, as their absorption tail through the visible range has been often detrimental to achieving good spectral rejection.[47–51]

With the aim of advancing the capabilities of organic narrowband photodetectors in the far-red range, in this study we investigate a non-fullerene route to overcoming the aforementioned limitations. This effort builds on the burgeoning of non-fullerene acceptors in the organic photovoltaics domain, where they have been gaining momentum in recent years as a promising alternative to mainstream Buckminsterfullerene and derivatives.[52–54] Here we recognize that the facile synthetic tailoring and ensuing spectral tunability of emerging non-fullerene acceptors also potentially provide a formidable opportunity for NBA photodetection. We thus explore the use of one such non-fullerene acceptor to realize solution-processible narrowband photodetectors for the far-red region. By incorporating this compound within different configurations of donor-acceptor bulk-heterojunction photoactive layers, we obtain fresh indications on the performance potential of the non-fullerene approach for the far-red range. We characterize our device implementations in regard to relevant performance metrics. By comparing our findings with the prior art, with find that our approach is cutting edge in regard to the spectral width and specific detectivity it delivers. Therefore, this study provides positive indications on the potential of non-fullerene acceptors for solution-processible organic narrowband photodetectors selective to the far red-region, thus expanding the scope of organic NBA photodetection.

2. Results and Discussion

With a view to developing NBA-type far-red organic photodetectors, we reasoned that emerging non-fullerene acceptors could provide a promising avenue, considering the small optical gap of many such compounds, in addition to their facile synthetic and spectral flexibility, as well as their ease of processing via solution-based methods.[52–54] This is specifically the case for compounds based on alternating donor-acceptor moieties, which can deliver strong absorption bands at photon energies below 2 eV due to their intramolecular charge transfer transitions.[55] The long-wavelength absorption band in any such compound, however, generally comes with an additional absorption band at shorter wavelengths due to the π−π* transition. While attractive for photovoltaics,[52,53] this higher-energy band has been recognized as problematic for organic narrowband photodetection, because it is detrimental to achieving good rejection of the photons in the intended photodetector stopband (i.e., spectral rejection).[11,56] In other words, non-fullerene acceptors for far-red-selective photodetection should ideally feature an intramolecular charge transfer band that is by-far preponderant over the π−π* counterpart.

In the search for a compound with the aforementioned properties for NBA-type far-red photodetection, we found a suitable candidate in SBDTIC (4,4,10,10-tetrakis(4-hexylphenyl)-5,11-(*n*-hexylthio)-4,10-dihydrodithienyl[1,2-*b*:4,5*b*']benzodi-thiophene-2,8-diyl)bis(2-(3-oxo-2,3-dihydroinden-1-ylidene)malononitrile), a small molecule recently developed for solar harvesting.[57] In brief, SBDTIC is a ladder-type benzodithiophene-based electron acceptor with an acceptor-donor-acceptor structure, as shown in **Figure 1**a. Films of SBDTIC deposited by spin-coating from a chloroform-based solution (as in **Figure 1**b) present the absorbance spectrum shown in **Figure 1**c. This spectrum manifests a composite fundamental band peaking at $\lambda_{p,\alpha}$ = 730 nm and with absorption full width at half maximum ($FWHM_\alpha$) of 132 nm (**Figure 1**c). This absorption band can be assigned to intramolecular charge transfer transitions. The fundamental absorption onset is at 777 nm, which denotes an optical gap of 1.60 eV. At

wavelengths shorter than the fundamental absorption band, the absorption spectrum presents a shallower band peaking at 483 nm (**Figure 1**c), which can be assigned to the π–π* transition. Notably, the latter band is particularly shallow, presenting an absorption ratio approaching 1:10 (after correcting for the background) with respect to the fundamental band. The location and spectral width of the fundamental absorption band, along with the limited absorption outside such band, suggest that SBDTIC is well poised for NBA photodetection in the far-red range. Additionally, photoluminescence (PL) spectroscopy reveals that SBDTIC films are strongly luminescent (**Figure 1**c), with a peak emission wavelength of 774 nm. This denotes an emissive excitonic state at the fundamental gap, which offers positive indications on the potential of SBDTIC for photoconversion.

In addition to its well-conditioned absorption and photoluminescence properties, SBDTIC also provides suitable electron transport. We obtained evidence of this from field-effect transistor measurements (**Figure 1**d). In a top-gate bottom-contact transistor (see Experimental Section for details on the fabrication procedure and data analysis), an electron mobility of up to $\approx 1 \cdot 10^{-2}$ $cm^2\ V^{-1}\ s^{-1}$ is obtained (**Figure 1**d). Along with the aforementioned optoelectronic properties, this substantiates the potential of SBDTIC as an acceptor for far-red photodetection.

To assess its narrowband photodetection capabilities, we integrated SBDTIC into a donor-acceptor (D-A) bulk-heterojunction (BHJ) photoactive layer. The first approach we considered aimed to combine SBDTIC with a donor having narrowband absorption also in the far-red range. We refer to this approach as *narrowband dual-absorber D-A*, as it relies on both donor and acceptor absorbing within the target spectral range (**Figure 2**a). Conceptually, this approach is attractive insofar as it maximizes the effective absorption coefficient of the photoactive layer within the target spectral range.

With a view to realizing an SBDTIC-based photodetector relying on the narrowband dual-absorber D-A concept, we conducted an extensive search among commercially available compounds that could potentially serve as donors while providing suitable absorption.

Conjugated polymers meeting both criteria could not be identified, as the ones with significant absorption in the far-red region generally possess a broadband character, which would prevent spectral selectivity in NBA photodetectors. In fact, we also faced a general lack of small-molecule candidates, as also confirmed by the paucity of the literature on far-red-selective NBA photodetectors (cf. the large number of small-molecule donors reported for NBA photodetection in the green and the blue ranges), as we found in our recent surveys of the area.[11,15] We found, however, that 2,4-Bis[4-(N,N-diisobutylamino)-2,6-dihydroxyphenyl] (DIBSQ, see **Figure 2**b), a squaraine molecule, could allow us to approximate the narrowband dual-absorber D-A configuration. This firstly follows from our assessment of the optical absorption properties of DIBSQ thin films. Such films present an absorption peak at 683 nm with a $FWHM_{\alpha}$ of 144 nm (**Figure 2**d), hence partly covering the far-red range. Their absorption onset (730 nm) corresponds to an optical gap of 1.7 eV, which is particularly close to that of SBDTIC. Additionally, its frontier energy levels[58] suggest that DIBSQ could potentially function as a donor with SBDTIC, in view of the type-II heterojunction formed at their interface (**Figure 2**c).

A DIBSQ:SBDTIC blend (1:1 by weight) spin-coated from chloroform present an absorption band peaking at 672 nm and with a $FWHM_{\alpha}$ of 161 nm (**Figure 2**d). This indicates that, while covering the far-red range, such absorption band also spans the red region. A comparison with the absorption spectra of DIBSQ and SBDTIC reveals that the absorption of the 1:1 blend is dominated by DIBSQ (as determined by its larger absorption coefficient, see **Figure S1**) yet SBDTIC contributes a significant shoulder within the main absorption band of the blend (which relates to the SBDTIC fundamental peak). A higher proportion of DIBSQ in the blend eventually results in the disappearance of the SBDTIC fundamental peak, resulting in a smaller $FWHM_{\alpha}$ (**Figure S2**). In contrast, a higher proportion of SBDTIC results in the broadening of the overall absorption spectrum, due to the emergence of the SBDTIC fundamental peak (**Figure S2**). All things considered, DIBSQ:SBDTIC films absorb throughout the red range,

including the far-red region. At the same time, their absorption in the green and blue regions is significantly smaller, hence they manifest a clear narrowband character. This makes them suitable for NBA photodetection, albeit only approximately realizing the aforementioned dual-absorber D-A concept for the far-red range, due to the imperfect spectral match between DIBSQ and SBDTIC.

For a preliminary assessment of the suitability of DIBSQ:SBDTIC films for photoconversion, we characterized their photoluminescence, which offers a window to their photogeneration process. The photoluminescence of DIBSQ:SBDTIC films is orders of magnitude lower than that of single-component SBDTIC films. This holds over a broad range of blend ratios (DIBSQ:SBDTIC from 4:1 to 1:4 by weight) and regardless of the predominance of one moiety or the other (**Figure 2**e). It is important to note that the PL spectra of DIBSQ-rich films does not allow one to conclude on the DIBSQ:SBDTIC capabilities for photocarrier generation. Indeed, their negligible photoluminescence may not necessarily originate from exciton dissociation at the DIBSQ-SBDTIC interface, as one has to also consider the limited luminescence of DIBSQ in the solid state (due to self-quenching, see **Figure S3**) and the limited proportion of excitons generated in inherently luminescent SBDTIC domains. On the other hand, the PL of SBDTIC-rich films indicates that exciton quenching can efficiently occur at the DIBSQ-SBDTIC interface. This offers a positive indication on the suitability of the SBDTIC-DIBSQ pair for photoconversion in a bulk heterojunction.

Photodetectors were fabricated by integrating DIBSQ:SBDTIC films (thickness ≈ 70 nm, see **Figure S4** for details) within a vertical device stack featuring indium tin oxide (ITO) and Aluminum (Al) as anode and cathode, respectively (**Figure 2**c). A poly(3,4-ethylenedioxythiophene) polystyrene sulfonate (PEDOT:PSS) film (thickness ≈ 50 nm, see **Figure S4** for details) was placed between the photoactive layer and the ITO anode to serve as a hole transport layer. Finally, a lithium fluoride (LiF) layer (≈ 1 nm thick) was inserted between the photoactive layer and the Al cathode to limit the dark current.

From the measurements of the photodetector current under illumination and in the dark, we determined the specific detectivity in the shot noise limit as $D^*(\lambda) = \left(I_{ph}(\lambda)/P_{opt}\right)/\sqrt{2qJ_d}$, where I_{ph} is the photocurrent (i.e., the difference between the total current measured under illumination, I_{tot}, and the total current measured in the dark, I_d, $I_{ph}(\lambda) = I_{tot}(\lambda) - I_d$), P_{opt} is the incident optical power, J_d is the dark current areal density ($J_d = 2.216 \cdot 10^{-5}\ mA\ cm^{-2}$ in self-powered mode, see **Figure S5**), q is the elementary charge, and λ is the wavelength of the incident light. As shown in **Figure 2**f, DIBSQ:SBDTIC photodetectors exhibit a clear detectivity band through the red and far-red ranges (consistently with the external quantum efficiency spectrum, see **Figure S6**), with a detectivity full width at half maximum ($FWHM_{D^*}$) of 186 nm. The maximum specific detectivity, $4.70 \cdot 10^{11}$ Jones, is reached at 740 nm. Concurrently, these photodetectors manifest considerably lower detectivity in the blue and the green regions. The shape of the detectivity spectrum reflects the combined absorption properties of DIBSQ and SBDTIC, the former predominant in the 600 – 700 nm range, and the latter in the 700 – 800 nm range. This implies that the appreciable detectivity width of DIBSQ:SBDTIC photodetectors directly relates to the imperfect spectral match of DIBSQ with respect to SBDTIC. Interestingly, while the longer-wavelength absorbance shoulder of SBDTIC is not predominant in the absorbance spectrum of the 1:1 blend, the maximum detectivity is achieved specifically in this range (**Figure 2**f). In view of the limited current choice of far-red-absorbing donors (e.g., see **Table S1** and references [11,15]), it can be anticipated that future synthetic efforts on the development of suitable donors may be able to improve the spectral performance of the narrowband dual-absorber D-A approach in the far-red range.

To overcome the spectral limitations of the narrowband dual-absorber D-A approach, we pursued an alternative strategy in which SBDTIC is blended with a donor that is transparent throughout the reference (i.e., visible) range (**Figure 4**a). We refer to this approach as *narrowband single-absorber D-A*, considering that only one compound in the blend absorbs in the target spectral range. The rationale of this approach lies in its ability to inherently prevent

the effects of any detrimental absorption mismatch between donor and acceptor, as found in the narrowband dual-absorber D-A configuration. Indeed, in single-absorber D-A, the absorbance width of the photoactive layer is set by the sole component that absorbs in the target spectral range, hence leading to minimal $FWHM_{\alpha}$ within a compositionally balanced D-A photoactive layer. Within the present work we implemented this approach by blending SBDTIC with poly[N,N'-bis(4-butylphenyl)-N,N'-bisphenylbenzidine] (PolyTPD), which serves as the transparent donor (**Figure 4**b-c). This choice follows from optical absorption and energetic considerations (*vide infra*), along with the facile solution processability and well-known hole-transport capabilities of PolyTPD.

PolyTPD:SBDTIC (1:1 by weight) films spin-coated from a chloroform solution exhibit an absorbance spectrum that is almost indistinguishable from that of SBDTIC films (**Figure 4**d). This originates from the negligible absorbance of PolyTPD through the reference (visible) range (simply presenting a marginal tail for wavelengths < 420 nm, **Figure 4**d), consistently with the aims of the narrowband single-absorber D-A approach. This enables blend films with an absorption band in the far-red region featuring a $FWHM_{\alpha}$ of 120 nm, i.e., appreciably smaller than that of the DIBSQ:SBDTIC case discussed earlier.

In order to ascertain the capability of PolyTPD-SBDTIC blend films to function as a D-A BHJ, we characterized their photoluminescence spectra (**Figure 4**e). Under excitation at λ_{ex} = 630 nm, blending SBDTIC with PolyTPD results in a significant reduction in PL intensity compared to the SBDTIC-only case. As excitons under λ_{ex} = 630 nm illumination are generated exclusively in the SBDTIC domains, this finding indicates that such excitons can be successfully dissociated within a PolyTPD:SBDTIC film, thus highlighting the capability of PolyTPD:SBDTIC to function as a D-A BHJ. Consequently, the residual photoluminescence intensity obtained from 1:1 films may be ascribed to some degree of phase separation in the PolyTPD:SBDTIC 1:1 films, which would lead to some excitons recombining radiatively prior to reaching the heterointerface.

On the basis of these findings, we realized PolyTPD:SBDTIC photodetectors by sandwiching PolyTPD:SBDTIC 1:1 films (thickness ≈ 110 nm, see **Figure S4** for details) between ITO/PEDOT:PSS and LiF/Al. Just as in the DIBSQ:SBDTIC case, we determined the specific detectivity of PolyTPD:SBDTIC 1:1 photodetectors in the shot noise limit (**Figure 4**f), considering that their measured dark current density amounts to $J_d = 5.947 \cdot 10^{-8}\ mA\ cm^{-2}$ in self-powered mode (see **Figure S5**). The specific detectivity spectrum closely follows the absorption spectrum of SBDTIC (and the external quantum efficiency spectrum, see **Figure S6**), consistently with the narrowband single-absorber D-A approach pursued here. In particular, this implies that these photodetectors primarily respond in the far-red region: the peak detectivity wavelength is at λ_{p,D^*} = 740 nm (compare with the peak absorption of SBDTIC at $\lambda_{p,\alpha}$ = 733 nm), and the predominant specific detectivity band has a width of $FWHM_{D^*}$ = 141 nm (compare with the absorption width $FWHM_{\alpha}$ = 132 nm of SBDTIC films) (**Figure 4**f). Additionally, we note that the absorption tail of PolyTPD in the visible range (up to ≈ 420 nm, see **Figure 3**d) does not result in a corresponding detectivity tail in the same spectral range. We attribute this to the limited photogeneration efficiency of photons absorbed in the PolyTPD domains, consistently with our PL data in **Figure S7**. This behavior is particularly advantageous in order to achieve good spectral rejection down to 400 nm. Importantly, we note that the specific detectivity of PolyTPD:SBDTIC photodetectors reaches a maximum of $1.42 \cdot 10^{13}$ Jones, which marks an increase of about two orders of magnitude compared to the DIBSQ:SBDTIC case. This dramatic improvement can be ascribed almost completely to a considerable reduction—by more than 3 orders of magnitude—of the photodetector dark current attained in PolyTPD:SBDTIC devices ($J_d = 5.947 \cdot 10^{-8}\ mA\ cm^{-2}$ versus $J_d = 2.216 \cdot 10^{-5}\ mA\ cm^{-2}$ of the DIBSQ:SBDTIC devices, as discussed earlier). (See **Table 1** for a direct comparison between the spectral characteristics of DIBSQ:SBDTIC and PolyTPD:SBDTIC devices.)

To put in context the results from PolyTPD:SBDTIC photodetectors, it is useful to consider how the detectivity and spectral width attained here compare to the prior literature on NBA

photodetectors sensitive in the red and far-red region (λ_{p,D^*} = 600 – 750 nm). We note that we consider here also red-responsive photodetectors in view of their spectral and material affinity with far-red photodetection. Such comparison is carried out in graphical form in **Figure 4**, which provides a plot of the peak specific detectivity D_p^* versus the $FWHM_{D^*}$ for all relevant works (as listed in detail in **Table S1** and found in our recent extensive surveys of the organic narrowband photodetector literature[11,15]). We have already noted that PolyTPD:SBDTIC photodetectors attain a smaller spectral width and a higher specific detectivity than the DIBSQ:SBDTIC counterpart. Here we additionally find that PolyTPD:SBDTIC photodetectors provide, to the best of our knowledge, the highest specific detectivity attained to date by NBA photodetectors sensitive in the red and far-red region. Additionally, we see that the spectral width (i.e., $FWHM_{D^*}$) of PolyTPD:SBDTIC photodetectors is significantly smaller than that of prior solution-processed implementations, bringing it down to 141 nm from 185 nm (lowest $FWHM_{D^*}$ of prior literature).[27,28,40–42,59] We note that a value of 141 nm is already suitable for a number of applications involving multispectral capability beyond the conventional red-green-blue (RGB) color space in the visible—e.g., such width value is comparable to those of commercial Foveon and CYMK imagers (**Figure S8**). While vacuum-processed implementations give smaller $FWHM_{D^*}$ values, this is in fact indicative of the general trend (also observed in other spectral regions) that NBA photodetectors typically give narrower spectral widths through vacuum-processed photoactive layers.[15] Considering that solution processing bears important advantages in terms of capital and manufacturing cost, as well as technological deployability, the spectral width reduction attained with solution-processed PolyTPD:SBDTIC compared to prior works marks an important step in this direction. This additionally highlights the performance edge of the NBA approach based on narrowband single-absorber D-A over its dual-absorber counterpart. Based on the spectral versatility of this approach, it can be envisaged that future developments in non-fullerene acceptors absorbing in

the far-red region and with reduced $FWHM_\alpha$ could lead to photodetectors with even narrower widths in this spectral range.

In addition to the performance characteristics discussed so far, narrowband photodetectors are also expected to maintain their photoconversion capability under variable power in order to be of practical use. We thus characterized the photocurrent response of both DIBSQ:SBDTIC and PolyTPD:SBDTIC photodetectors under illumination of power density in the $\approx 10^{-3} - 10^{2}$ mW cm^{-2} range and under an applied bias of 0 V. We found that the photocurrent in both device types is approximately linear with optical power ($J_{ph} \propto P_{opt}^{r}$ with $r \approx 1$) over the measured power range (which spans nearly 5 orders of magnitude). Based on the probed optical power range (determined by the experimental constraints on the optical power of our source), both DIBSQ:SBDTIC and PolyTPD:SBDTIC photodetectors exhibit a linear dynamic range (LDR) of at least 77.9 dB. (Here, LDR is calculated as $LDR := 20\log_{10}\left(i_{ph,max}/i_{ph,min}\right)$, where $i_{ph,max}$ and $i_{ph,min}$ are the observed endpoints of the range over which the $P_{opt} - i_{ph}$ characteristics are linear.) We note that that these figures likely underestimate the actual LDR, as the $i_{ph,min}$ values considered here are limited by the optical power we can source with our apparatus. From a device physics point of view, such trend can be related to photoconversion operating under one-center recombination.[60,61] At a technological level, the near-linearity of the photoresponse confirms the suitability of our photodetectors to function under a broad range of optical power values.

The transient response of a photodetector is a further aspect defining its performance and applicability scope. The transient response of both DIBSQ:SBDTIC and PolyTPD:SBDTIC photodetectors was characterized firstly under pulsed illumination of variable power. Representative photocurrent traces are presented in **Figure 5**b. From the photocurrent transients we extracted the rise and fall times corresponding to 50% of the full transitions (**Figure 5**c), which we indicate as $t_{rise}^{(50)}$ and $t_{fall}^{(50)}$. We found that the two device types (DIBSQ:SBDTIC and

PolyTPD:SBDTIC) deliver nearly overlapping rise times and fall times. The rise time is practically unchanged with optical power, while the fall time is marginally reduced (by approximately 20% over a change in optical power of an order of magnitude). In particular, by averaging over the probed optical power range, the fall time is ≈ 1.2 μs, while the rise time is ≈ 3 μs. This corresponds to a response time—defined as the arithmetic average of the rise and fall times, $t_r^{(50)} = \left(t_{rise}^{(50)} + t_{fall}^{(50)}\right)/2$ —of approximately 2.1 μs. In regard to the asymmetry between the fall and rise time and their dependence on optical power, both may be traced to carrier trapping effects. In the Bube-Rose framework consistent with our $P_{opt} - i_{ph}$ characteristics,[60] the slight reduction of the fall time with optical power can be rationalized with the presence of a uniform trap distribution superimposed on the dominant recombination center.[61] As the optical power and the quasi-free carrier density increase, the impact of such traps is reduced, resulting in a shorter fall time. Within such framework, the asymmetry between rise and fall times may then be attributed to a difference between the carrier capture rate on the rising edge of the transient and the carrier emission rate on the falling edge of the transient.

We additionally characterized the transient response of our photodetectors by monitoring their photocurrent response under sinusoidally-modulated incident optical power (superposed on continuous wave illumination). The resulting (normalized) photocurrent is presented in **Figure 5**d. The corresponding 3dB frequency f_{3dB} (at which the photocurrent is reduced by a factor of $\sqrt{2}$ with respect to the low-frequency value) amounts to 129.5 kHz for DIBSQ:SBDTIC and 118.3 kHz for PolyTPD:SBDTIC. The similar 3dB frequency values are in accord with the near-indistinguishable rise times and fall times observed under pulsed illumination. The inverse of $t_r^{(50)}$ is approximately within a factor of 2 of the f_{3dB} values, confirming the consistency of the transient response under pulsed and modulated illumination. Such operating speeds under pulsed and modulated illumination are in compliance with the requirements of the target applications of NBA far-red photodetection. Not only can these photodetectors operate at

frequencies compatible with still-image acquisition, but in fact can also be relied upon for high-speed video acquisition, e.g., in the context of a multispectral camera.

3. Conclusions

Aiming to expand the scope of the highly-attractive narrowband absorption (NBA) approach to spectrally-selective organic photodetection, in this work we have pursued a fullerene-free avenue for the far-red range in order to overcome the spectral limitations of the prior art. We have specifically focused on solution-processible SBDTIC, an acceptor-donor-acceptor benzodithiophene-based electron acceptor. We have shown that such compound features a spectrally suitable absorption peak (at 730 nm) for NBA far-red photodetection, as well as an attractively limited spectral width (132 nm) of its fundamental absorption band, and a marked preponderance of the latter with respect to the higher-energy π–π^* band ($\approx$ 10:1 in strength). To assess its narrowband photodetection potential, we have considered two approaches to realizing SBDTIC-based bulk-heterojunction NBA photodetectors: one comprising a squaraine donor, DIBSQ, absorbing also in the far-red range, and another involving a transparent donor, PolyTPD. We have found that PolyTPD:SBDTIC photodetectors offer superior narrowband photodetection performance, in view of their ability to prevent any optoelectronic broadening arising from an imperfect spectral match between donor and acceptor in a BHJ. In particular, we have shown that PolyTPD:SBDTIC photodetectors are responsive in the far-red range, delivering a peak specific detectivity in the shot noise limit of $1.42 \cdot 10^{13}$ and a spectral width of 141 nm in self-powered mode. To the best of our knowledge, these values constitute the highest specific detectivity to date for NBA far-red-selective photodetectors, and the smallest spectral width of all such solution-processed implementations. We have additionally characterized these photodetectors in respect to their linearity under variable-power illumination and their transient response to pulsed and modulated illumination. This has allowed us to show that such

photodetectors are in compliance with the operational requirements underlying relevant applications in the far-red range. In perspective, this work has shown that non-fullerene acceptors offer a promising avenue for NBA photodetection beyond conventional colour bands—e.g., in the far-red and at longer wavelengths. In particular, while synthetic efforts in non-fullerene acceptor research have thus far mainly focused on photovoltaics, our results point to the attractiveness of such compounds also for narrowband photodetection, and motivate dedicated synthetic efforts in this direction.

4. Experimental Section

Materials. SBDTIC was synthesized according to the same procedure detailed by Lin et al.[57] The following chemicals were purchased and used without further purification: DIBSQ (97%, Sigma-Aldrich), PolyTPD (MW > 10000, Lumtec), Polystyrene (average MW 35000, Sigma-Aldrich), PEDOT:PSS (Clevios P VP Al 4083, Heraeus), chloroform (≥ 99.8%, HPLC, Yonghua Chemical Co., Ltd), acetone (≥ 99.5%, AR, Sinopharm Chemical Reagent Co., Ltd), isopropanol (≥ 99.7%, AR, Yonghua Chemical Co., Ltd), LiF (99.99%, Zhongnuoxincai, Beijing Technology Co., Ltd), Al (99.999%, Zhongnuoxincai, Beijing Technology Co., Ltd). ITO coated glass substrates were purchased from South China Science & Technology Co., Ltd. Glass substrates were purchased from Guangzhou Lighting Glass Co., Ltd.

Solution preparation. Solutions of PolyTPD, DIBSQ and SBDTIC and their blends were prepared by dissolution of their powders in chloroform within a nitrogen-filled glove box. In regard to blends used for device fabrication, each compound was dissolved at a concentration of 10 mg/mL. Prior to processing, solutions were stirred for 4 hours at 40 ℃.

Photodetector fabrication. ITO-coated glass substrates were cleaned via an ultrasonic bath sequentially in acetone, isopropanol and deionized water for 15 minutes. After drying in

nitrogen flow, the substrates were treated with oxygen plasma (Harrick, PDC-002). After filtering (PTFE filter, 0.45 μm pore size), PEDOT:PSS was spin-coated (500 rpm for 15 s, 3000 rpm for 30 s) on the treated substrates, and the samples were then annealed on a hot plate at 150 ℃ for 10 min. The photoactive layer solution was then spin-coated (2500 rpm for 40 s, 1000 rpm for 20 s) onto the samples, which were then annealed at 50 ℃ /80 ℃ for 5 min. Finally, 1.5 nm LiF and 80 nm Al layers were thermally evaporated onto the samples at a pressure below $2 \cdot 10^{-6}$ mbar through a shadow mask.

Transistor Fabrication. Glass substrates were cleaned sequentially via an ultrasonic bath sequentially in acetone, isopropanol and deionized water for 15 minutes. After drying in nitrogen flow, the substrates were treated with oxygen plasma (Harrick, PDC-002). Chromium/gold (2nm/20nm) source and drain electrodes were thermally evaporated in high vacuum and patterned via standard lift-off photolithography, following the same procedure reported in Ref. [62]. SBDTIC (dissolved in chloroform, as for photodetector fabrication) was then spin-coated, followed by the spin-coating of a 620 nm-thick CYTOP film (subsequently annealed at 90 ℃ for 20 min). Finally, Al gate electrodes (50 nm thick) were deposited by thermal evaporation through a shadow mask. The saturation mobility was extracted as: $\mu_{sat} = 2 \cdot L \cdot \left(\partial\sqrt{I_{DS}}/\partial V_{GS}\right)^2/(WC_d)$, where I_{DS} is the drain-source current, V_{GS} the gate-source voltage, W the channel width, L the channel length, and C_d the areal capacitance of the gate dielectric.

Characterization. Ultraviolet-visible-near-infrared (UV-Vis-NIR) absorption spectra of organic semiconductor films on quartz were measured with a UV-Vis-NIR LAMBDA 750 spectrophotometer (PerkinElmer). Steady-state photoluminescence spectra were measured with a FL3 fluorometer (HORIBA Scientific). Thickness values of spin-coated organic films were measured with a Veeco Multimode V atomic force microscope (Bruker) in tapping mode, using

a silicon cantilever (Nanoworld, NCH) with a nominal radius of < 8 nm. Photodetector current-voltage characteristics were measured in air with a Keithley 6420 source meter, while transistor characteristics were acquired with a 4200A-SCS semiconductor parameter analyzer (Tektronix). Photocurrent spectra were measured with a custom-built setup comprising an Omni-λ2005i monochromator (Zolix) and a power meter (Thorlabs, PM200) with a calibrated silicon sensor (Thorlabs, S120VC). Variable-power and transient photocurrent measurements were conducted with a custom-built setup relying on a 624 nm LED source, controlled with a USB-6001 data acquisition device (National Instruments) through a LabVIEW program, and with the current signal amplified by a DHPCA-100 amplifier (FEMTO).

Supporting Information
Supporting Information is available from the Wiley Online Library or from the author.

Acknowledgements
K. X. and V. P. have contributed equally to this work. The authors gratefully acknowledge financial support from the National Natural Science Foundation of China (61750110517 and 61805166), the Jiangsu Province Natural Science Foundation (BK20170345), the Collaborative Innovation Center of Suzhou Nano Science & Technology, the Priority Academic Program Development of Jiangsu Higher Education Institutions (PAPD), the 111 Project, and the Joint International Research Laboratory of Carbon-Based Functional Materials and Devices. The authors are also very grateful to Jiu-Dong Lin and Prof. Liang-Sheng Liao for kindly providing the SBDTIC used in this study. Finally, the authors are thankful to Vladimir Kremnican for his technical support with the measuring apparatus.

Author Contributions
K. X. carried out the bulk of the fabrication and characterization experiments. V. P. and K. X. designed and assembled the photocurrent and transient photocurrent setups. Y. L. and W. Y. carried out the transistor fabrication, characterization, and data analysis. L. P. helped with the transistor data analysis. V. P. conceived and supervised the project, designed the experiments, carried out the data analysis, and wrote the manuscript. All authors discussed the results and revised the manuscript.

Conflict of Interest
The authors declare no conflict of interest.

References

[1] Y. Wu, K. Fukuda, T. Yokota, T. Someya, *Adv. Mater.* **2019**, *31*, 1903687.

[2] F. Cao, J. Chen, D. Yu, S. Wang, X. Xu, J. Liu, Z. Han, B. Huang, Y. Gu, K. L. Choy, H. Zeng, *Adv. Mater.* **2019**, 1905362.

[3] Z. Zhao, J. Wang, C. Xu, K. Yang, F. Zhao, K. Wang, X. Zhang, F. Zhang, *J. Phys. Chem. Lett.* **2019**, 366.

[4] Q. Lin, A. Armin, P. L. Burn, P. Meredith, *Nat. Photonics* **2015**, *9*, 687.

[5] W. Wang, F. Zhang, M. Du, L. Li, M. Zhang, K. Wang, Y. Wang, B. Hu, Y. Fang, J. Huang, *Nano Lett.* **2017**, *17*, 1995.

[6] F. P. García de Arquer, A. Armin, P. Meredith, E. H. Sargent, *Nat. Rev. Mater.* **2017**, *2*, 16100.

[7] Z. Zhao, C. Li, L. Shen, X. Zhang, F. Zhang, *Nanoscale* **2020**, *12*, 1091.

[8] J. Miao, F. Zhang, *Laser Photon. Rev.* **2018**, *13*, 1800204.

[9] R. D. Jansen-van Vuuren, A. Armin, A. K. Pandey, P. L. Burn, P. Meredith, *Adv. Mater.* **2016**, *28*, 4766.

[10] K. J. Baeg, M. Binda, D. Natali, M. Caironi, Y. Y. Noh, *Adv. Mater.* **2013**, *25*, 4267.

[11] V. Pecunia, *Organic Narrowband Photodetectors: Materials, Devices and Applications*, Institute Of Physics Publishing, Bristol, UK, **2019**.

[12] C. L. Chochos, S. A. Choulis, *Prog. Polym. Sci.* **2011**, *36*, 1326.

[13] G. P. and A. G. and M. S. and D. N. and M. Caironi, *Semicond. Sci. Technol.* **2015**, *30*, 104006.

[14] K. Takei, in *Flex. Stretchable Med. Devices*, Wiley-VCH Verlag GmbH & Co. KGaA, Weinheim, Germany, **2018**, pp. 1–6.

[15] V. Pecunia, *J. Phys. Mater.* **2019**, *2*, 042001.

[16] P. C. Y. Chow, T. Someya, *Adv. Mater.* **2019**, 1902045.

[17] S. Cai, X. Xu, W. Yang, J. Chen, X. Fang, *Adv. Mater.* **2019**, *31*, 1808138.

[18] S.-T. Han, H. Peng, Q. Sun, S. Venkatesh, K.-S. Chung, S. C. Lau, Y. Zhou, V. A. L. Roy, *Adv. Mater.* **2017**, *29*, 1700375.

[19] R. Jansen van Vuuren, K. D. Johnstone, S. Ratnasingam, H. Barcena, P. C. Deakin, A. K. Pandey, P. L. Burn, S. Collins, I. D. W. Samuel, *Appl. Phys. Lett.* **2010**, *96*, 253303.

[20] K. Takei, Ed. , *Flexible and Stretchable Medical Devices*, Wiley-VCH Verlag GmbH & Co. KGaA, Weinheim, Germany, **2018**.

[21] A. Armin, R. D. Jansen-Van Vuuren, N. Kopidakis, P. L. Burn, P. Meredith, *Nat. Commun.* **2015**, *6*, 6343.

[22] W. Wang, M. Du, M. Zhang, J. Miao, Y. Fang, F. Zhang, *Adv. Opt. Mater.* **2018**, *6*, 1800249.

[23] Z. Tang, Z. Ma, A. Sánchez-Díaz, S. Ullbrich, Y. Liu, B. Siegmund, A. Mischok, K. Leo, M. Campoy-Quiles, W. Li, K. Vandewal, *Adv. Mater.* **2017**, *29*, 1702184.

[24] Y. Sato, H. Kajii, Y. Ohmori, *Org. Electron.* **2014**, *15*, 1753.

[25] W. Li, H. Guo, Z. Wang, G. Dong, *J. Phys. Chem. C* **2017**, *121*, 15333.

[26] K. H. Lee, D. S. Leem, J. S. Castrucci, K. B. Park, X. Bulliard, K. S. Kim, Y. W. Jin, S. Lee, T. P. Bender, S. Y. Park, *ACS Appl. Mater. Interfaces* **2013**, *5*, 13089.

[27] T. Sakai, H. Seo, T. Takagi, H. Ohtake, *MRS Adv.* **2016**, *1*, 459.

[28] W. Li, S. Li, L. Duan, H. Chen, L. Wang, G. Dong, Z. Xu, *Org. Electron.* **2016**, *37*, 346.

[29] T. Sakai, H. Seo, T. Takagi, M. Kubota, H. Ohtake, M. Furuta, in *2015 IEEE Int. Electron Devices Meet.*, IEEE, **2015**, pp. 30.3.1-30.3.4.

[30] T. Takagi, H. Seo, T. Sakai, H. Ohtake, M. Furuta, *Electron. Imaging* **2016**, *2016*, 1.

[31] H. Seo, S. Aihara, T. Watabe, H. Ohtake, M. Kubota, N. Egami, *Jpn. J. Appl. Phys.* **2007**, *46*, L1240.

[32] Z. Yang, B. Rutherford, R. McDonald, J. P. Houston, *IEEE J. Sel. Top. Quantum Electron.* **2017**, *23*, 59.

[33] G. P. Liao, S. D. Olson, D. J. Kota, R. A. Hetz, P. Smith, S. Bedi, C. S. Cox, *J. Surg. Res.* **2014**, *190*, 628.

[34] T. D. O'Sullivan, R. T. Heitz, N. Parashurama, D. B. Barkin, B. A. Wooley, S. S. Gambhir, J. S. Harris, O. Levi, *Biomed. Opt. Express* **2013**, *4*, 1332.

[35] S. Wieneke, H. Ahrends, A. Damm, F. Pinto, A. Stadler, M. Rossini, U. Rascher, *Remote Sens. Environ.* **2016**, *184*, 654.

[36] F. Fiorani, U. Rascher, S. Jahnke, U. Schurr, *Curr. Opin. Biotechnol.* **2012**, *23*, 227.

[37] K. Bürling, Z. G. Cerovic, G. Cornic, J. M. Ducruet, G. Noga, M. Hunsche, *Environ. Exp. Bot.* **2013**, *89*, 51.

[38] M. Teena, A. Manickavasagan, A. Mothershaw, S. El Hadi, D. S. Jayas, *Food Bioprocess Technol.* **2013**, *6*, 1621.

[39] H. Seo, S. Aihara, T. Watabe, H. Ohtake, T. Sakai, M. Kubota, N. Egami, T. Hiramatsu, T. Matsuda, M. Furuta, T. Hirao, *Jpn. J. Appl. Phys.* **2011**, *50*, 024103.

[40] S. Z. Hassan, H. J. Cheon, C. Choi, S. Yoon, M. Kang, J. Cho, Y. H. Jang, S. K. Kwon, D. S. Chung, Y. H. Kim, *ACS Appl. Mater. Interfaces* **2019**, *11*, 28106.

[41] C. W. Joo, J. Kim, J. Moon, K. M. Lee, J. E. Pi, S. Y. Kang, S. D. Ahn, Y. S. Park, D. S. Chung, *Org. Electron.* **2019**, *70*, 101.

[42] H. Opoku, B. Lim, E. Shin, H. Kong, J. M. Park, C. Bathula, Y. Noh, *Macromol. Chem. Phys.* **2019**, *220*, 1900287.

[43] J. Y. Kim, P. Vincent, J. Jang, M. S. Jang, M. Choi, J. H. Bae, C. Lee, H. Kim, *J. Alloys Compd.* **2020**, *813*, 152202.

[44] S. Aihara, Y. Hirano, T. Tajima, K. Tanioka, M. Abe, N. Saito, N. Kamata, D. Terunuma, *Appl. Phys. Lett.* **2003**, *82*, 511.

[45] S. Aihara, Y. Hirano, T. Tajima, K. Miyakawa, Y. Ohkawa, T. Matsubara, T. Takahata, S. Suzuki, N. Egami, K. Tanioka, M. Abe, N. Saito, N. Kamata, D. Terunuma, *2003 IEEE Work. CCD Adv. Image Sensors* **2003**, 8.

[46] T. Sakai, H. Seo, S. Aihara, M. Kubota, M. Furuta, in *Sensors, Cameras, Syst. Ind. Sci. Appl. XIV* (Eds.: R. Widenhorn, A. Dupret), **2013**, *8659*, 86590G.

[47] X. Bulliard, Y. W. Jin, G. H. Lee, S. Yun, D. Leem, T. Ro, K. Park, C. Heo, R. Satoh, T. Yagi, Y. S. Choi, S. J. Lim, S. Lee, *J. Mater. Chem. C* **2016**, *4*, 1117.

[48] R. Satoh, T. Ro, C. Heo, G. H. Lee, W. Xianyu, Y. Park, J. Park, S. Lim, D. Leem, X. Bulliard, Y. Kim, K. Bae, W. Yang, K. Park, Y. W. Jin, S. Lee, *Org. Electron.* **2017**, *41*, 259.

[49] S. Heo, J. Lee, S. H. Kim, D. J. Yun, J. B. Park, K. Kim, N. Kim, Y. Kim, D. Lee, K. S. Kim, H. J. Kang, *Sci. Rep.* **2017**, *7*, 1516.

[50] M. G. Han, K. B. Park, X. Bulliard, G. H. Lee, S. Yun, D. S. Leem, C. J. Heo, T. Yagi, R. Sakurai, T. Ro, S. J. Lim, S. Sul, K. Na, J. Ahn, Y. W. Jin, S. Lee, *ACS Appl. Mater. Interfaces* **2016**, *8*, 26143.

[51] R. D. Jansen-van Vuuren, A. Pivrikas, A. K. Pandey, P. L. Burn, *J. Mater. Chem. C* **2013**, *1*, 3532.

[52] J. Hou, O. Inganäs, R. H. Friend, F. Gao, *Nat. Mater.* **2018**, *17*, 119.

[53] C. Yan, S. Barlow, Z. Wang, H. Yan, A. K. Y. Jen, S. R. Marder, X. Zhan, *Nat. Rev. Mater.* **2018**, *3*, 18003.

[54] Z. Q. Jiang, T. T. Wang, F. P. Wu, J. D. Lin, L. S. Liao, *J. Mater. Chem. A* **2018**, *6*, 17256.

[55] A. Köhler, H. Bässler, in *Electron. Process. Org. Semicond.*, Wiley-VCH Verlag GmbH & Co. KGaA, Weinheim, Germany, **2015**, pp. 87–191.

[56] S. Yoon, C. W. Koh, H. Y. Woo, D. S. Chung, *Adv. Opt. Mater.* **2018**, *6*, 1.

[57] J. D. Lin, L. Zhong, F. P. Wu, Y. Li, Y. Yuan, H. Bin, Z. Zhang, F. Liu, J. Fan, Z. G. Zhang, L. S. Liao, Z. Q. Jiang, Y. Li, *Sci. China Chem.* **2018**, *61*, 1405.

[58] G. Chen, H. Sasabe, Z. Wang, X. F. Wang, Z. Hong, Y. Yang, J. Kido, *Adv. Mater.* **2012**, *24*, 2768.

[59] W. Li, D. Li, G. Dong, L. Duan, J. Sun, D. Zhang, L. Wang, *Laser Photon. Rev.* **2016**, *10*, 473.

[60] R. H. Bube, in *Photoelectron. Prop. Semicond.*, Cambridge University Press, Cambridge, UK, **1992**, pp. 45–59.

[61] A. Rose, in *Concepts Photocond. Allied Probl.*, John Wiley & Sons, New York, NY, USA, **1963**, pp. 11–68.

[62] V. Pecunia, M. Nikolka, A. Sou, I. Nasrallah, A. Y. Amin, I. McCulloch, H. Sirringhaus, *Adv. Mater.* **2017**, *29*, 1606938.

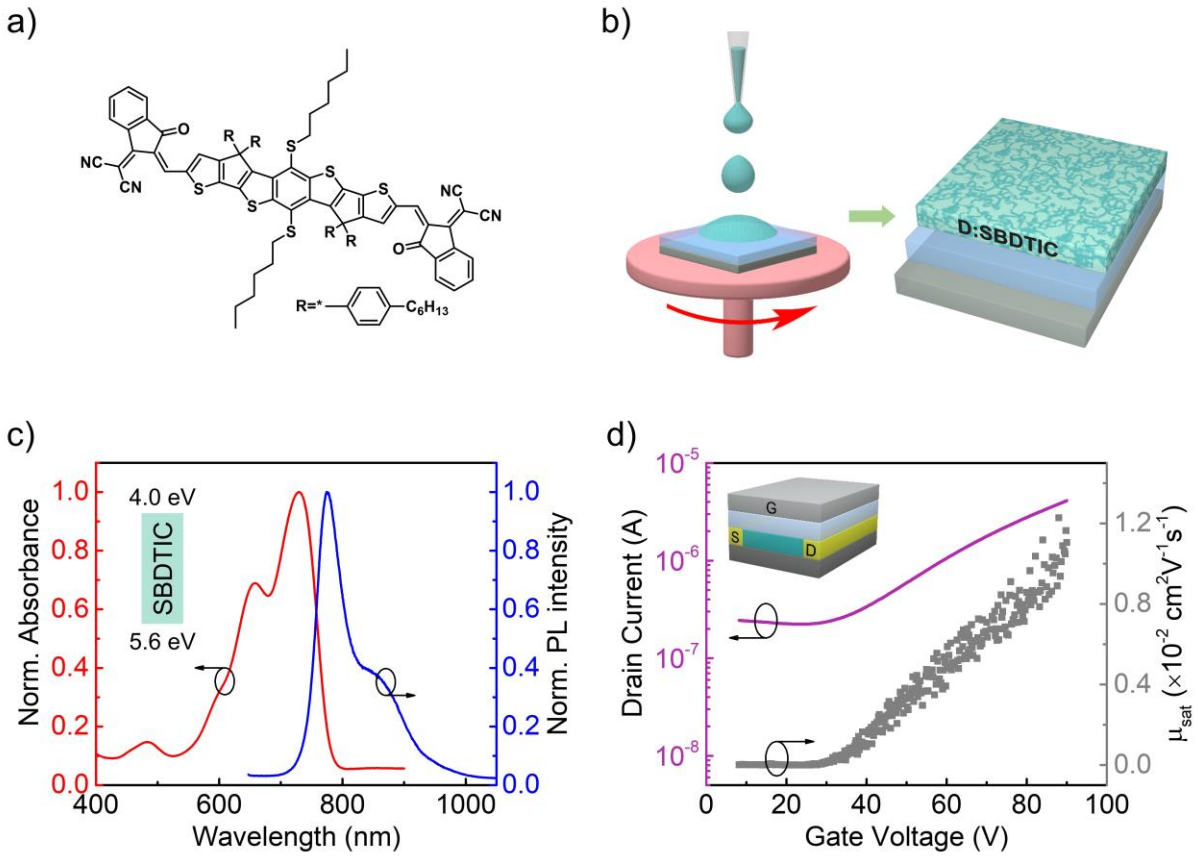

Figure 1 a) Molecular structure of SBDTIC. b) Schematic illustration of the spin-coating of SBDTIC, alone or in a blend with other soluble compounds, e.g., a donor of choice. c) Absorption and photoluminescence spectra (excitation wavelength λ_{ex}= 630 nm) of SBDTIC thin films (inset: literature values of frontier energy levels). d) Current-voltage characteristic and carrier mobility of SBDTIC from a field-effect-transistor measurement (inset: device structure).

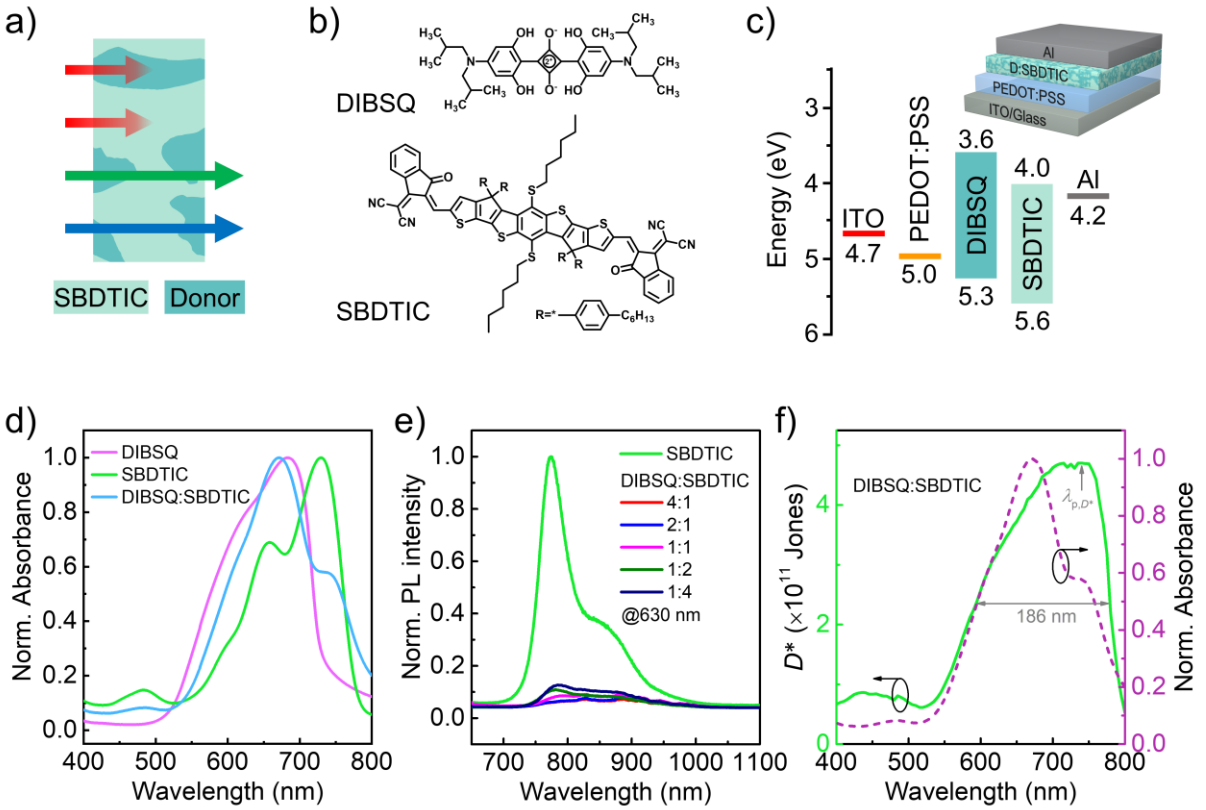

Figure 2 a) Illustration of the narrowband dual-absorber D-A concept for far-red NBA photodetection. Photons in the target spectral range are represented with red arrows, while photons in other spectral regions are represented with blue and green arrows. b) Molecular structure of the donor (DIBSQ) and the acceptor (SBDTIC) used to approximate the dual-absorber D-A approach in the far-red range. c) Schematic depiction of the device structure and the key energy levels of the layers in the device stack. d) Normalized thin-film absorption spectra of DIBSQ, SBDTIC, and DIBSQ:SBDTIC (1:1 by weight). e) PL spectra of SBDTIC films and DIBSQ:SBDTIC films with different blend ratios (excitation wavelength λ_{ex} = 630 nm). f) Specific detectivity spectrum of DIBSQ:SBDTIC photodetectors and normalized thin-film absorption spectrum of DIBSQ:SBDTIC (1:1 by weight).

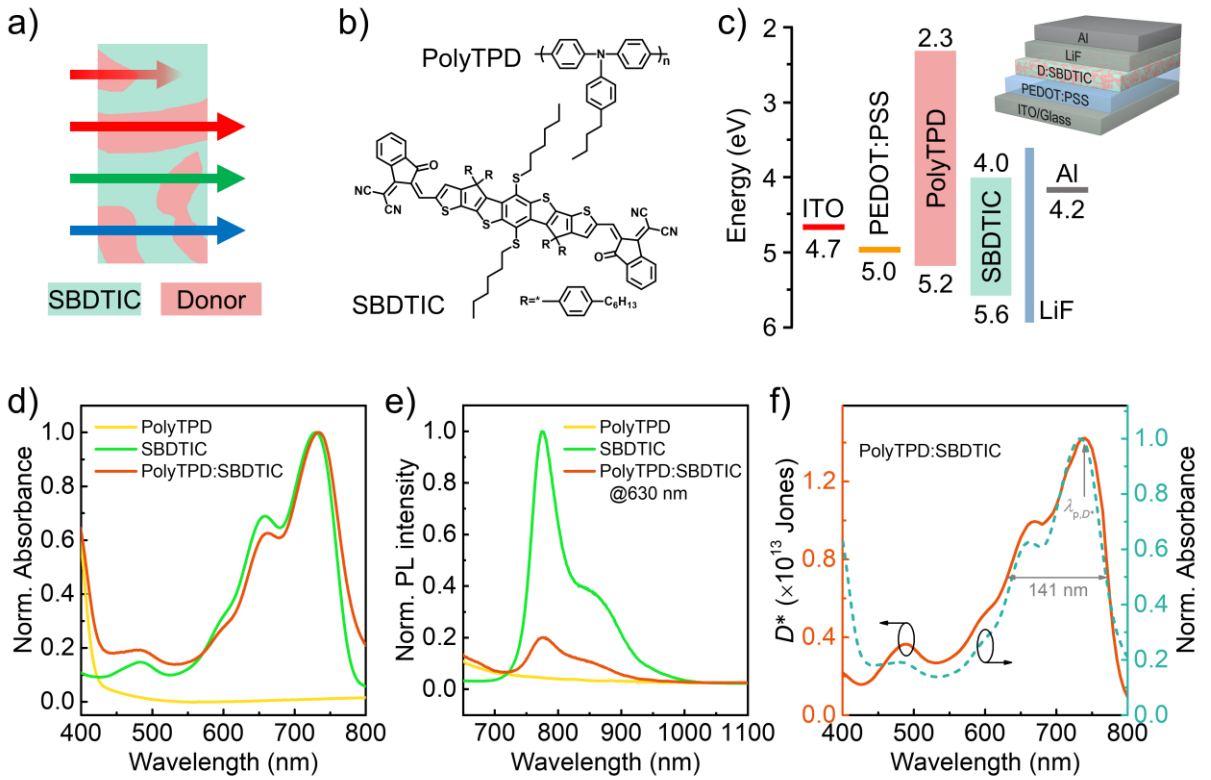

Figure 3 a) Illustration of the narrowband single-absorber D-A concept for far-red NBA photodetection. Here the donor is transparent to photons of all wavelengths in the reference spectral range (denoted with blue, green, and red arrows), while the acceptor selectively absorbs in the target spectral range (denoted here with a red arrow). b) Molecular structure of the donor (PolyTPD) and the acceptor (SBDTIC) used for the single-absorber D-A approach pursued in this work. c) Schematic depiction of device structure and key energy levels of the different layers in the device stack. d) Normalized thin-film absorption spectra of PolyTPD, SBDTIC, and PolyTPD:SBDTIC (1:1 by weight). e) Photoluminescence spectra of PolyTPD, SBDTIC, and PolyTPD:SBDTIC films (excitation wavelength λ_{ex} = 630 nm). f) Specific detectivity spectra of PolyTPD:SBDTIC photodetectors and normalized thin-film absorption spectra of PolyTPD:SBDTIC (1:1 by weight).

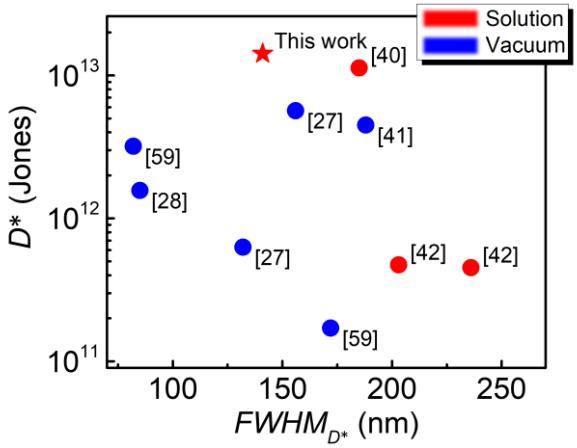

Figure 4 Specific detectivity and its spectral width from the literature on NBA photodetectors sensitive in the red region (λ_{p,D^*} = 675 – 755 nm). The peak specific detectivity values presented here are in the shot noise limit (see Table S1 for details). The PolyTPD:SBDTIC devices reported in this work attain the highest specific-detectivity in the shot noise limit, and constitute the solution-processed implementation with the narrowest spectral width.

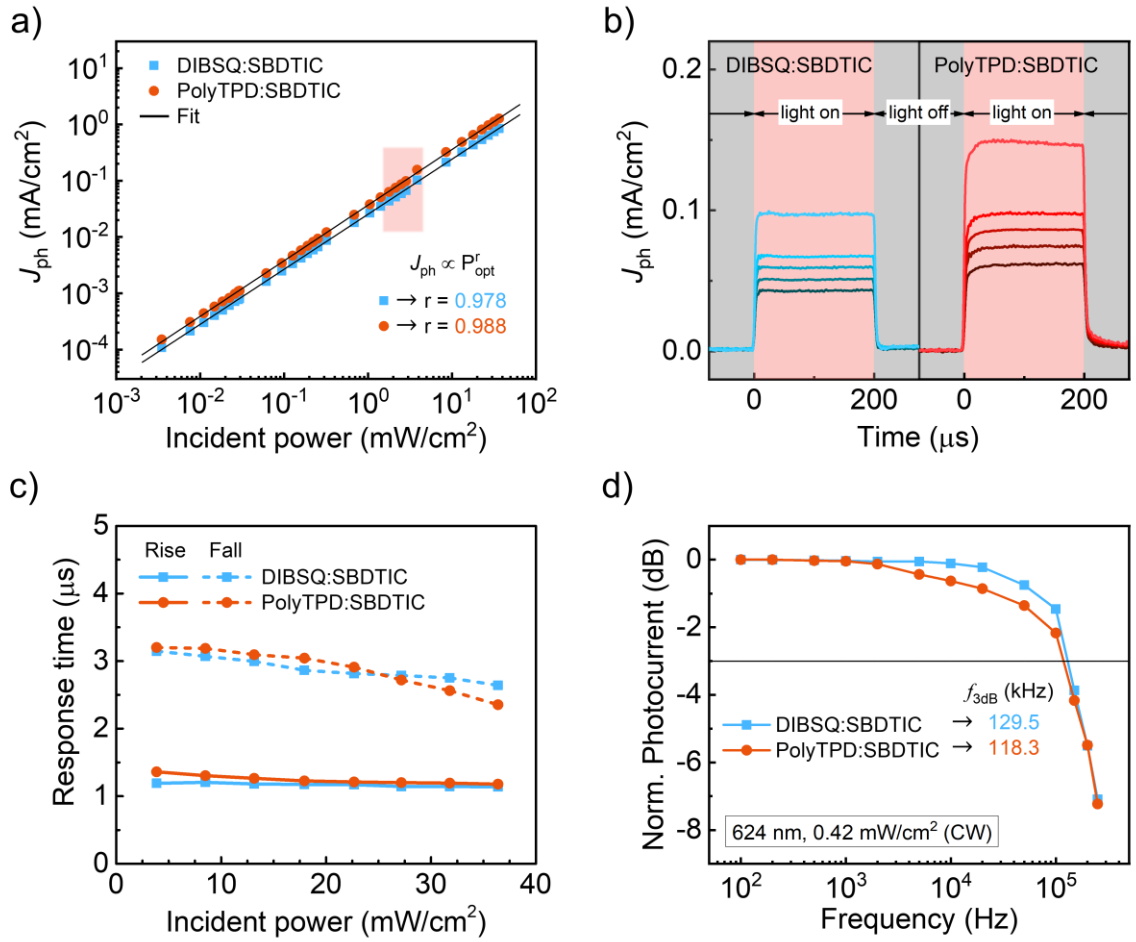

Figure 5 a) Photocurrent density J_{ph} versus optical power density P_{opt} in DIBSQ:SBDTIC and PolyTPD:SBDTIC devices. A fit of the type $J_{ph} \propto P_{opt}^{r}$ is overlaid on the measured datasets, with the corresponding best-fit exponent r values being listed in the bottom right corner. b) Photocurrent response to a pulsed illumination (pulse duration equal to 200 µs) for both DIBSQ:SBDTIC and PolyTPD:SBDTIC devices. The optical power values at which these traces were acquired correspond to the shaded area in a). c) Fall and rise time extracted as a function of P_{opt} extracted from the pulse response in c) for both DIBSQ:SBDTIC and PolyTPD:SBDTIC devices. d) Modulated responsivity (normalized) as a function of the modulation frequency for both DIBSQ:SBDTIC and PolyTPD:SBDTIC devices. These measurements were carried out under illumination at a wavelength of 624 nm, with the modulated optical signal superposed on a continuous-wave illumination of power density 0.42 mW/cm^2. The corresponding f_{3dB} values are indicated in the legend.

Table 1. Spectral characteristics of the photodetectors presented in this work. All parameters are as defined in the text. In addition: D_p^* is peak specific detectivity; λ_{p,D^*} is the wavelength of maximum specific detectivity ; $\lambda_{p,\alpha}$ is the wavelength of maximum absorption.

Photoactive material	D_p^*	$FWHM_{D^*}$	λ_{p,D^*}	$FWHM_{\alpha}$	$\lambda_{p,\alpha}$
	Jones	nm	nm	nm	nm
DIBSQ:SBDTIC	$4.70\ 10^{11}$	186	740	161	672
PolyTPD:SBDTIC	$1.42\ 10^{13}$	141	740	120	732